OPEN ACCESS
IOP Publishing | International Atomic Energy Agency
Nuclear Fusion
Nucl. Fusion **65** (2025) 056039 (18pp)
https://doi.org/10.1088/1741-4326/adce19

Impact of shape and global β on ASDEX Upgrade pedestal structure

L. Radovanovic[1,*], E. Wolfrum[2], M.G. Dunne[2], G.F. Harrer[3], F. Aumayr[1] and the ASDEX Upgrade Team[a]

[1] Institute of Applied Physics, TU Wien, Fusion@ÖAW, Wiedner Hauptstr. 8-10, 1040 Vienna, Austria
[2] Max Planck Institute for Plasma Physics, Boltzmannstraße 2, 85748 Garching, Germany
[3] Department of Physics, Hampton University, 268 Emancipation Drive, VA 23668, United States of America

E-mail: radovanovic@iap.tuwien.ac.at

Received 29 August 2024, revised 26 March 2025
Accepted for publication 17 April 2025
Published 28 April 2025

Abstract

The stability and confinement of the pedestal, the outermost region of the confined plasma in a tokamak, are crucial for its efficient operation and performance. This work describes ASDEX Upgrade experiments designed to analyse the pedestal structure under varying conditions of normalized poloidal pressure (β_{pol}) and plasma shaping. The individual treatment of temperature, density, and pressure for ion and electron pedestals is emphasized. We show that the ion temperature (T_{i}) increases with β_{pol}, whereas the electron temperature (T_{e}) shows only a slight increase and the electron density (n_{e}) remains relatively unaffected. The changes in shape influence n_{e}, making its pedestal higher and wider, whereas T_{i} remains unchanged despite a lower heating power required to keep the same β_{pol} at high shaping. The findings highlight the importance of distinguishing between different channels when predicting and controlling the pedestal. The stabilising influence of the radial electric field E_{r}, and its correlation with different pedestal top positions, is explored. The roles of ballooning modes and local magnetic shear are emphasized, and the conditions for access to second stability in different pedestal regions are presented. The global MHD stability sets the overall limit, but the radial composition of electron density and electron and ion temperature can strongly vary. The results show that the width of the electron pressure pedestal is determined by the equilibrium via the local magnetic shear. The strongest correlation of the ion pressure pedestal top position is found with the gradient of E_{r}. We found that the second stability access requires both a highly shaped boundary and a q profile modification due to higher pressure gradients. The results contribute to understanding the mechanisms governing the pedestal behaviour, offering insights for optimizing plasma performance and stability.

Keywords: plasma physics, magnetohydrodynamics, pedestal, ballooning modes, second stability, radial electric field

(Some figures may appear in colour only in the online journal)

[a] See Zohm *et al* 2024 (https://doi.org/10.1088/1741-4326/ad249d) for the ASDEX Upgrade Team.
[*] Author to whom any correspondence should be addressed.

1. Introduction

The stability and confinement of tokamak plasmas in the high-confinement mode (H-mode) [1] are strongly influenced by the pedestal, the edge of the confined plasma. While turbulence governs radial transport in the core, it is reduced in the pedestal by $E \times B$ shear from the radial electric field E_r [2], described by:

$$E_r = \frac{\nabla p}{n_i Z_i e} - v_{i,\mathrm{pol}} B_{\mathrm{tor}} + v_{i,\mathrm{tor}} B_{\mathrm{pol}}, \tag{1}$$

where ∇p is the pressure gradient, Z the charge number, e the elementary charge, v_{pol} and v_{tor} the poloidal and toroidal rotation, and B_{tor} and B_{pol} the toroidal and poloidal magnetic fields for ion species i. The current theoretical picture is that $E \times B$ shear elongates turbulent eddies, reducing radial transport and making neoclassical transport dominant. Since E_r and ∇p are interdependent, this creates a self-sustaining system constrained by transport and magnetohydrodynamic (MHD) stability limits.

In this study, we examine the role that E_r and global MHD have on the pedestal structure, but also highlight on the role that local MHD stability has on the pedestal width, conducting separate investigations into ions and electrons. We aim to identify two key parameters that enable control of the pedestal structure. The first is the poloidal normalised plasma pressure, β_{pol}, which characterises the global ratio between plasma pressure and magnetic pressure. This parameter is known to significantly influence pedestal behaviour [3–5] and is closely linked to the stability of kinetic ballooning modes (KBMs), which are critical for pedestal stability [5, 6]. The second parameter is the plasma shape, particularly the upper triangularity, δ_{up}. Plasma shaping affects both local and global MHD stability by shifting the stability boundary [7–10]. The adjustability of both parameters on ASDEX Upgrade provides a practical experimental advantage.

For reference, we outline the existing models currently used to predict pedestal behaviour in the following section. In section 3, we articulate the hypotheses underlying the experiments, describe the experimental setup, and provide a comprehensive overview of the discharges performed on ASDEX Upgrade. The workflow, including the tools employed in the process, is also described. Section 4 provides measurements of the ion and electron kinetic profiles in the plasma edge, emphasizing the changes in the pedestal width and gradient. In section 5 MHD stability of the discharges is explored, highlighting the correlation between the ideal $n \to \infty$ ballooning modes, radial electric field E_{r}, and the pedestal top positions of electron pressure p_{e}, ion pressure p_{i} and total pressure p. Finally, in section 6, the findings are discussed, and possible further investigations are suggested.

2. Background on present pedestal models

The pedestal structure is approximately defined by its gradient and its width, and its characteristics play a crucial role in determining the overall behaviour of the plasma. Various approaches are employed to model this structure, with the EPED [11] model being a commonly used one, and more recently, integrated modelling (IMEP) uses a pedestal model based on engineering parameters for ASDEX Upgrade [12, 13]. One shared characteristics between these two models is that they both determine the pedestal width and height using the intersection between two limitations: MHD stability and some transport constraint.

The MHD constraint in both models relies on the ideal peeling-ballooning stability limit, which, when crossed, triggers an Edge Localised Mode (ELM) [14]. During these periodic events particles and energy are lost, the pedestal ‘crashes’, and after a few milliseconds it is recovered, so the cycle repeats. Using this limit, it is possible to capture the maximum pedestal width and height, just before the ELM onset. However, this method does not address the limits on the pedestal between ELMs. Furthermore, it makes it challenging to predict pedestals of ELM-free regimes [15].

The IMEP modelling approach uses transport simulations which determine the pressure at the pedestal top, for a given pedestal width, as described in [12]. The simulation makes use of the empirical findings in [16], which shows that the electron temperature gradient length ($T_{\mathrm{e}}/\nabla T_{\mathrm{e}}$) in real space coordinates, when scaled to the machine size, remains the same across multiple machines (AUG, JET and DIII-D). This scaling is consistent over plasma shapes, heating powers and electron densities, and it is assumed that the limit is set by electron temperature gradient modes (ETGs), however, this has not yet been shown.

The transport limitation in EPED is based on the observed connection between the pedestal width (Δ_{ped}) and the normalized poloidal pressure ($\beta_{\mathrm{pol}} = < p > / p_{\mathrm{mag}}$) which is defined as the ratio between the global plasma pressure ($< p > = < n k_{\mathrm{B}} T >$) and the poloidal magnetic pressure ($p_{\mathrm{mag}} = B_{\mathrm{p}}/2\mu_0$).

The EPED model hypothesizes that a particular kind of instability, the KBM, imposes a constraint on a critical normalized pressure gradient. Considering β_{pol} as a driving force for KBMs, as well as stabilizing through the generation of bootstrap current and its impact on the magnetic shear, leads to a dependence of $\Delta_{\mathrm{ped}} = D \cdot \sqrt{\beta_{\mathrm{pol}}}$. With its several adaptations and extensions, the model has been successful in describing pedestal width and height across a range of experiments.

The foundations of the EPED model, β_{pol} and shaping, have been extensively investigated across multiple tokamaks [17]. Specific studies have reported that lower squareness can lead to higher pressure [5], and a double-null configuration has been found to result in a wider pedestal [18] On JET, access to the second stability regime enhances the pedestal and improves confinement [19], while higher shaping has been linked to increased pedestal height both on JET [20], DIII-D [5] and JT-60U [21, 22].

However, while often a useful model its limitations are that the factor D depends on multiple parameters such as the regime of operation, shaping of the plasma, and collisionality, making it difficult to predict the pedestal without experimental data to base the scaling constant on. Additionally, it is assumed that the electron and ion pedestals of temperature and density are governed by the same, or several strongly coupled mechanisms, which is not necessarily the case as shown at DIII-D [23] and JET [20]. The same observation will also be highlighted in the following analysis, and it indicates that a simple pressure scaling may not fully capture the underlying physics of pedestal formation.

Although the $\beta_{\mathrm{pol,ped}}$ scaling often provides a reasonable description of pedestal width, there are notable exceptions. For instance, in JET with a beryllium wall and a tungsten divertor at high gas fuelling and high shaping, the pedestal width does not follow the $\beta_{\mathrm{pol,ped}}$ scaling [24, 25]. Similarly, in DIII-D QH-mode, the pedestal width is significantly larger than expected [18]. Early studies on the DIII-D tokamak [10] demonstrated that higher shaping leads to increased pedestal pressure. However, the correlation between pedestal width and $\sqrt{\beta_{\mathrm{pol,ped}}}$ was weak, and it was suggested that access to the second stability region might play a role. These cases indicate that additional effects, beyond a simple $\beta_{\mathrm{pol,ped}}$ scaling, may influence pedestal structure and confinement.

Furthermore, in conjunction with the EPED model, a relationship between KBMs, MHD, and pedestal width was also shown on MAST during the inter-ELM evolution of the pedestal [26]. In more recent studies of pedestals in an ELM-free, quasi-continuous exhaust (QCE) regime on ASDEX Upgrade, stability calculations show that ideal $n \to \infty$ ballooning modes, which are commonly used as a proxy for KBMs, are close to the stability boundary in the pedestal [27, 28]. In that work, and here, three regions of the pedestal are differentiated: top, middle, and foot. While in the QCE regime, the pedestal foot ($\rho > 0.99$) is prominently ballooning unstable, and the pedestal top region also approaches the stability limit. The stability of the steepest region, the pedestal middle, depends on the magnetic shear. At low global shear and high pressure gradient, the pedestal middle is in the second stable regime and stable against ballooning modes. This effect plays an important role in the following analysis and will be further discussed in sections 5.2 and 5.3.

Given the strong dependence of KBMs on β and shaping, and the extensive studies of these relationships in multiple tokamaks, this work aims to further investigate how shaping affects pedestal structure and stability. In the following sections, we explore these dependencies in our dataset and assess how they compare to previous findings.

3. Experimental setup

3.1. Triangularity and β_{pol} variation

Three ASDEX Upgrade discharges are compared in this study: #38472, #38474 and #38819 and their overall properties are listed in table 1. All three discharges are at a plasma current I_{p} of 800 kA in an type-I ELMy H-mode. The magnetic field varies slightly, and it is −2.5 T for #38472 and #38474, and −2.7 T in #38819. The heating changes due are to the β_{pol} feedback, ranging from 6 to 12 MW for #38472, 6.1–8.7 MW for #38474 and 4–9 MW for #38819. The safety factor at 95% flux q_{95} has relatively similar values, ranging from 5.1 in the low triangularity to 6 in the high triangularity phases. The confinement time τ_{E} ranges from 0.05 s in all three low shaping discharges to 0.07 s in the medium β_{pol} discharge in the high shaping phase. All discharges are fuelled with $8 \cdot 10^{21}\ \mathrm{s}^{-1}$ deuterium gas puff.

The plasma shape is known to substantially affect the pedestal structure. It is commonly observed that increasing plasma shaping increases its global peeling–ballooning MHD stability limit toward higher pressure gradients, therefore allowing for higher pedestal top values. We explore this effect further and additionally look into the effect of the plasma shape on the local ideal ballooning modes (IBMs). The ballooning modes are a particular kind of instability, located typically at the low field side (LFS) of the plasma. They are driven by the pressure gradient and stabilised by the square of the magnetic shear, which is defined as $s = \mathrm{d}q/\mathrm{d}r\ r/q$ where q is the safety factor and r the minor radius. By changing the upper triangularity (δ_{up}) and elongation (κ) we substantially influence the local magnetic shear which is stabilising the local IBMs. The implications for the pedestal width are studied by conducting discharges, in which two time-windows with different plasma shapes are analysed. In each of the three discharges, at 4 s a shape transition is made from lower shaping ($\delta_{\mathrm{up}} = 0.1$, $\kappa = 1.6$) to higher shaping ($\delta_{\mathrm{up}} = 0.25$, $\kappa = 1.7$) as can be seen in figure 1(*a*).

The normalised plasma pressure, β_{pol} is suggested to be another factor that plays a crucial role in the pedestal width [6]. In order to examine this pedestal property, each of the discharges is set to have a different fixed β_{pol}. To achieve this, we use β_{pol} feedback: a tool which is based on the flexible neutral beam injection (NBI) heating system that adjusts the total plasma pressure as the magnetic pressure changes, and keeps a constant β_{pol}. Despite constant total plasma pressure, the pedestal values can significantly vary, as can be seen in the following analysis.

Over discharges, β_{pol} is set to vary as follows: #38472 high $\beta_{\mathrm{pol}} = 1.35$, #38474 medium $\beta_{\mathrm{pol}} = 1.15$, #38819 low $\beta_{\mathrm{pol}} = 1.0$, and the measured values are shown in figure 1(*b*). While the feedback worked very well in the low and high beta case, it is notable that the discharge #38474 shows slight differences in β_{pol} in the two phases, both values are however in the medium range.

For discharge #38472 in figure 2, we focus on the time intervals of 2.8–3.0 s and 5.3–5.5 s for further analysis, as indicated by the grey stripes in the figure. A significant instability occurs around 6 s, causing notable perturbations in the plasma. Panel (*a*) emphasizes the NBI power in green, showing a baseline level of NBI power, while the flexible beam exhibits a comb-like pattern, toggling on and off to maintain a constant poloidal beta (β_p) of 1.3. This regulation proves effective, as illustrated in panel (*c*), where β_{pol} is depicted in purple. However, the total NBI heating during the second high-shaping phase is lower than in the first. In panel (*b*) it is notable that after the shape change at 4 s both core and edge density significantly increase.

Table 1. Plasma properties overview.

	β_{pol}	$\beta_{\mathrm{pol,ped}}$	β_{N}	I_{P}	B_{T}	heating power	q_{95}	τ_{E}
#38472	1.35	0.127, 0.178	1.95	800 kA	−2.5 T	6–12 MW	5.1, 5.6	0.05, 0.06
#38474	1.1–1.15	0.105, 0.154	1.6	800 kA	−2.5 T	6.1–8.7 MW	5.1, 5.6	0.05, 0.07
#38819	1	0.098, 0.137	1.3	800 kA	−2.7 T	4–9 MW	5.5, 6	0.05, 0.05

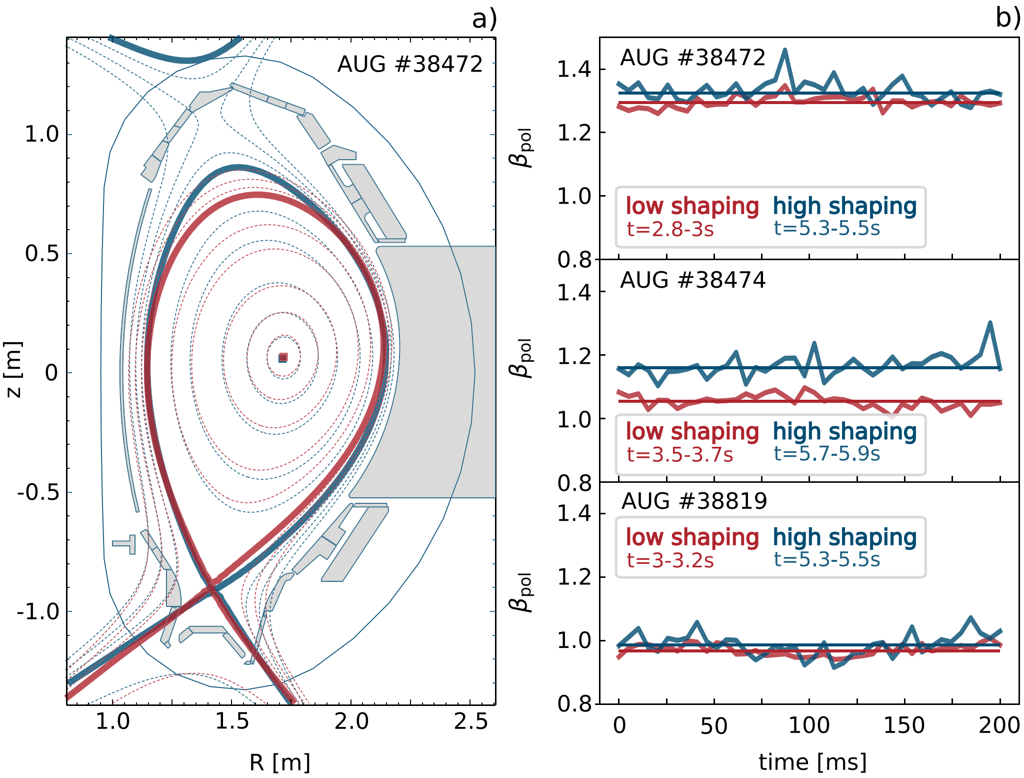

Figure 1. Experimental setup of the three analysed ASDEX Upgrade discharges, in (*a*) the cross-section of the plasma depicting the shape variation for each discharge, red lines represent the low shaping phases and blue lines the high shaping phases. The variation of β_{pol} for the 200 ms time windows is shown in (*b*) in decreasing order, with the horizontal line marking the median value for the window.

Panel (*d*) shows the yellow curve representing δ_{up}, which increases between 4 and 5 s, reflecting a deliberate alteration in plasma shape. This change has an immediate and significant impact on electron density (n_e), with substantial increases in both core and edge densities. Additionally, there is a slight rise in elongation k, indicating a shift in the plasma's overall structure.

In discharge #38474 (figure 3), we selected time windows of 3.5–3.7 s for the low shaping phase and 5.7–5.9 s for the high shaping phase, marked by grey stripes. The conditions are largely consistent with the previous discharge, with the main difference being a poloidal beta (β_{pol}) of 1.1, resulting in reduced NBI heating. In this case, β_{pol} is not as well matched as in discharge #38472, likely because the flexible NBI beam had already been turned off, leaving only the baseline contribution. As a result, β_{pol} remains slightly higher in the high shaping phase than in the low shaping phase, though the difference is minimal.

For the final discharge #38819 in figure 4, we utilized a slightly higher toroidal magnetic field (B_t) of 2.7 T compared to 2.5 T in the previous cases. The shape remained consistent, but a lower β_{pol} target of 1.0 was aimed for throughout the discharge, which was achieved consistently. A minor increase in radiative power occurred at 5.7 s, just before the selected time window, due to a core mode, which did not affect the pedestal significantly; for instance, the magnetic stored energy (W_{MHD}) in (*c*) remained unchanged, the edge density shown in purple in (*b*) stayed at the same value, and only the core density had a decrease, ensuring stable pedestal conditions. For this discharge, we selected time windows of 3.0–3.2 s for the low shaping phase and 5.7–5.9 s for the high shaping phase.

Figure 5 presents the divertor shunt current I_{polSOLa} for the three analysed discharges, with #38472 shown in panels (*a*) and (*b*), #38474 in (*c*) and (*d*), and #38819 in (*e*) and (*f*). The left panels correspond to the low-shaping phases, while the right panels show the high-shaping phases. Additionally, the stored MHD energy is plotted in orange on the right *y*-axis. The grey vertical stripes mark the phases that were excluded from the analysis. It can be observed that in all three discharges, the low-shaping phases exhibit a higher ELM frequency compared to the high-shaping phases. Furthermore, a general trend is seen where the ELM frequency decreases as β_{pol} decreases,

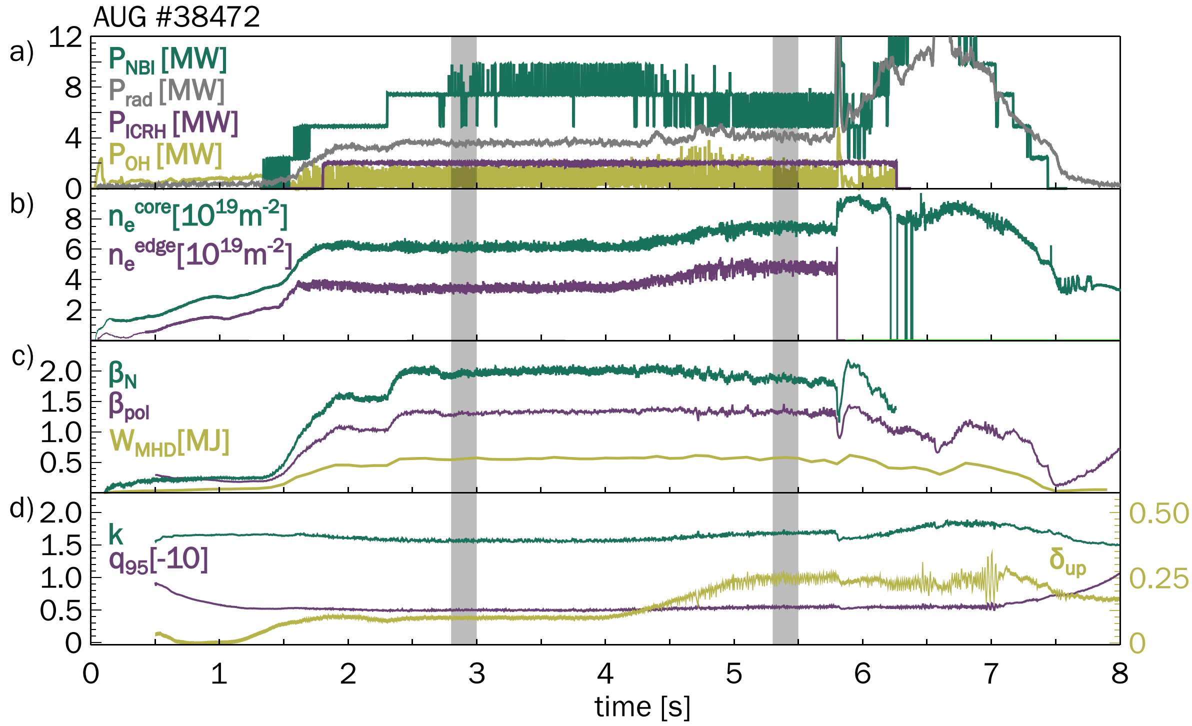

Figure 2. The figure shows time traces of some key quantities for discharge #38472. Panel (*a*) illustrates the contributions to heating power: neutral beam injection (NBI) power P_{NBI} (green), ohmic heating P_{OH} (yellow), and ion cyclotron resonance heating (ICRH) power P_{ICRH}, along with the radiative power P_{rad} (gray). Panel (*c*) presents the density data from DCN diagnostics, indicating core (green) and edge (purple) line-integrated densities. Panel (*d*) features the normalized beta β_N (green), poloidal beta β_p (purple), and the stored magnetic energy W_{MHD} (yellow). Lastly, panel (*e*) shows the elongation *k* (green), the safety factor *q* at $\psi_n = 0.95$ (purple, scaled by -10), and the upper triangularity δ_{up} (yellow, right axis).

indicating that β_{pol} plays a role in setting the ELM behaviour in these plasmas.

Having presented some initial results, we can see how the chosen β_{pol} range was determined within its constraints. As shown in figure 5(*a*), further increasing β_{pol} would result in even higher ELM frequencies, which would disrupt the analysis. Conversely, in order to maintain as many parameters as possible unchanged, we aimed to keep the plasma current the same across all three discharges for a consistent comparison. Alternatively, it is possible to reduce the heating power further. However, as illustrated in figure 4, in the high-shaping case, the heating power is already quite low, posing the risk of transitioning back into L-mode. Given these constraints, the β_{pol} range was chosen to be 1–1.35 under the given conditions.

3.2. Workflow

The workflow for this analysis starts with the plasma measurements of electron density n_{e} (deuterium cyanide laser interferometry [29], Thomson scattering [30]), electron temperature T_{e} (Thomson scattering, electron cyclotron emission spectroscopy [31]) and ion temperature T_{i} (charge exchange recombination spectroscopy [32, 33]), while the ion density is calculated using n_{e} and the effective charge number Z_{eff}. The information about these physical parameters is forward modelled using Bayesian probability theory in the Integrated Data Analysis of electrons/ions (IDA/IDI) [34].

The equilibrium is then reconstructed, coupled with the flux diffusion equation in IDA for Equilibrium reconstruction (IDE) [35]. The profiles and equilibria are created every 5 ms of the discharge. Each analysed time window is 200 ms long and selected so that it contains the highest quality of diagnostics measurements. All discharges are affected by the type-I ELMs, with frequency ranging from 100 Hz to 200 Hz. The phases most strongly influenced by an ELM crash, specifically, 1 ms before and 3 ms after, are filtered out, and the remaining inter-ELM period is considered for analysis, with averaging performed over this interval. After the ELM filtering, the profiles are averaged so that all following profiles show the median as a full line and the 95% of the results as a shaded area. In the analysis we focus on the pedestal, where we differentiate between several regions: *separatrix*—the last closed flux surface, *pedestal foot*—region just inside the separatrix, typically $0.99 < \rho_{\mathrm{pol}} < 1$, *pedestal middle*—the steep gradient region, typically $0.975 < \rho_{\mathrm{pol}} < 0.99$, *pedestal top*—radial position of the 'knee' of the pedestal, typically around $0.965 < \rho_{\mathrm{pol}} < 0.975$, and outer core—flat gradient region, typically at $\rho_{\mathrm{pol}} < 0.96$.

IDE provides input for the HELENA code [36]: the pressure gradient along the normalised flux $\mathrm{d}p/\mathrm{d}\psi$, diamagnetic profile $\mathrm{FdF/d}\psi$, with $\mathrm{F} = \mathrm{RB_T}$ and the flux surface at $\Psi_N = 0.995$ defining the plasma boundary. HELENA then solves the Grad-Shafranov equation to reconstruct the equilibrium in high resolution. The Suydam method [37] is performed

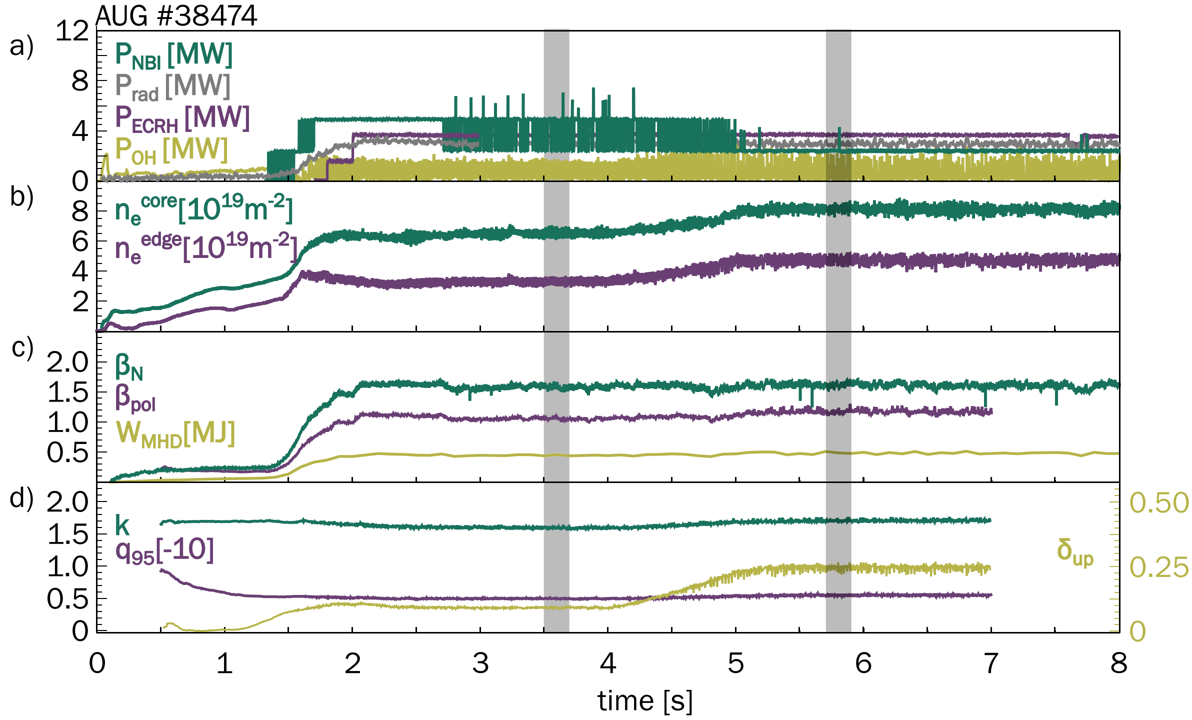

Figure 3. The figure shows time traces of some key quantities for discharge #38474. Panel (*a*) illustrates the contributions to heating power: neutral beam injection (NBI) power P_{NBI} (green), ohmic heating P_{OH} (yellow), and electron cyclotron resonance heating (ECRH) power P_{ECRH}, along with the radiative power P_{rad} (gray). Panel (*b*) presents the density data from DCN diagnostics, indicating core (green) and edge (purple) line-integrated densities. Panel (*c*) features the normalized beta β_N (green), poloidal beta β_p (purple), and the stored magnetic energy W_{MHD} (yellow). Lastly, panel (*d*) shows the elongation k (green), the safety factor q at $\psi_n = 0.95$ (purple, scaled by -10), and the upper triangularity δ_{up} (yellow, right axis).

on this high resolution equilibrium to solve the n $\rightarrow \infty$ ideal ballooning stability of the plasma. The MISHKA code [38] is later used to determine the global peeling—ballooning stability. The outcome of the computation with HELENA yields three distinct quantities: global surface averaged magnetic shear—stabilising the modes, experimental normalised pressure gradient α_{exp} defined as

$$\alpha = -2\mu_0 \frac{\partial V}{\partial \psi} \frac{1}{(2\pi)^2} \left(\frac{V}{2\pi^2 R_0}\right)^{1/2} \frac{\partial p}{\partial \psi} \tag{2}$$

where μ_0 is vacuum permeability, V is the plasma volume, ψ is the mean flux, and R_0 the large plasma radius, and the critical value of α at which the plasma becomes ballooning unstable α_{crit} and the ratio of the two quantities is defined as $F_{\mathrm{marg}} = \alpha_{\mathrm{crit}}/\alpha_{\mathrm{exp}}$, which indicates how close the plasma is to the ballooning instability. IDE also gives the input for calculating the local magnetic shear for a qualitative two-dimensional study of its stabilising effects, shown in section 5.3.

The CXRS diagnostics is used to self-consistently calculate the radial electric field E_r [33] by measuring the radiation from impurity ions, specifically boron, which results from charge exchange reactions between ionized impurity ions and injected beam neutrals. The intensity of this radiation provides information about the impurity density. Additionally, the temperature of the impurity ions is determined from the Doppler broadening of the spectral lines. These two measurements together are used to calculate the diamagnetic term of E_r. The velocity of the impurity ions is derived from the Doppler shifts observed in the poloidally and toroidally measured spectra. This enables the calculation of E_r for the impurity ions solely from CXRS measurements. Since E_r is consistent across all ion species, even though individual components vary, the E_r calculated for the impurity ions is also valid for the main ions. The reconstructed E_r profiles are then binned for the chosen time windows, the phases just after an ELM crash are filtered out, and the remaining data is fitted with a Gaussian process fit.

4. Kinetic profiles

The first step in this analysis is to compare the ion temperature T_i, electron temperature T_e, electron density n_e electron pressure p_e profiles at the plasma edge, as a function of the normalised pressure β_{pol}. For this, the low triangularity phase in the three selected discharges (#38819 $\beta_{\mathrm{pol}} = 1.0$ shown in green, #38474 $\beta_{\mathrm{pol}} = 1.1$ shown in orange and #38472 $\beta_{\mathrm{pol}} = 1.3$ shown in black) is chosen. Time windows of 200 ms are taken, ELM phases are filtered out, and the median is shown as full lines, and the shaded areas represent 95% quantiles. Figure 6(*a*) shows that the ion temperature T_i increases with the increase in β_{pol}. The total value of T_i at the separatrix and the core is higher, and in the discharge with the highest β_{pol} a slight increase in the T_i gradient is also observable.

The electron temperature T_e, shown in figure 6(*b*) shows a significant change only in the outer core region ($0.94 < \rho_{\mathrm{pol}} <$

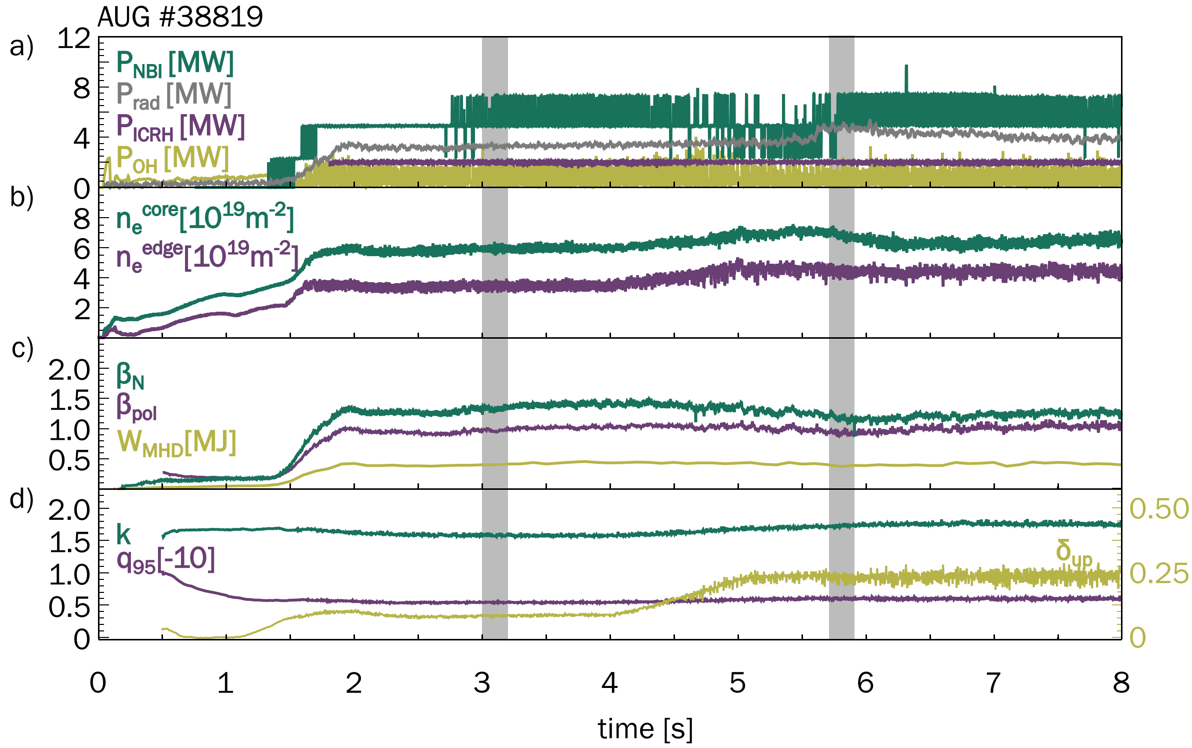

Figure 4. The figure shows time traces of some key quantities for discharge #38819. Panel (*a*) illustrates the contributions to heating power: neutral beam injection (NBI) power P_{NBI} (green), ohmic heating P_{OH} (yellow), and ion cyclotron resonance heating (ICRH) power P_{ICRH}, along with the radiative power P_{rad} (gray). Panel (*b*) presents the density data from DCN diagnostics, indicating core (green) and edge (purple) line-integrated densities. Panel (*c*) features the normalized beta β_N (green), poloidal beta β_p (purple), and the stored magnetic energy W_{MHD} (yellow). Lastly, panel (*d*) shows the elongation k (green), the safety factor q at $\psi_n = 0.95$ (purple, scaled by -10), and the upper triangularity δ_{up} (yellow, right axis).

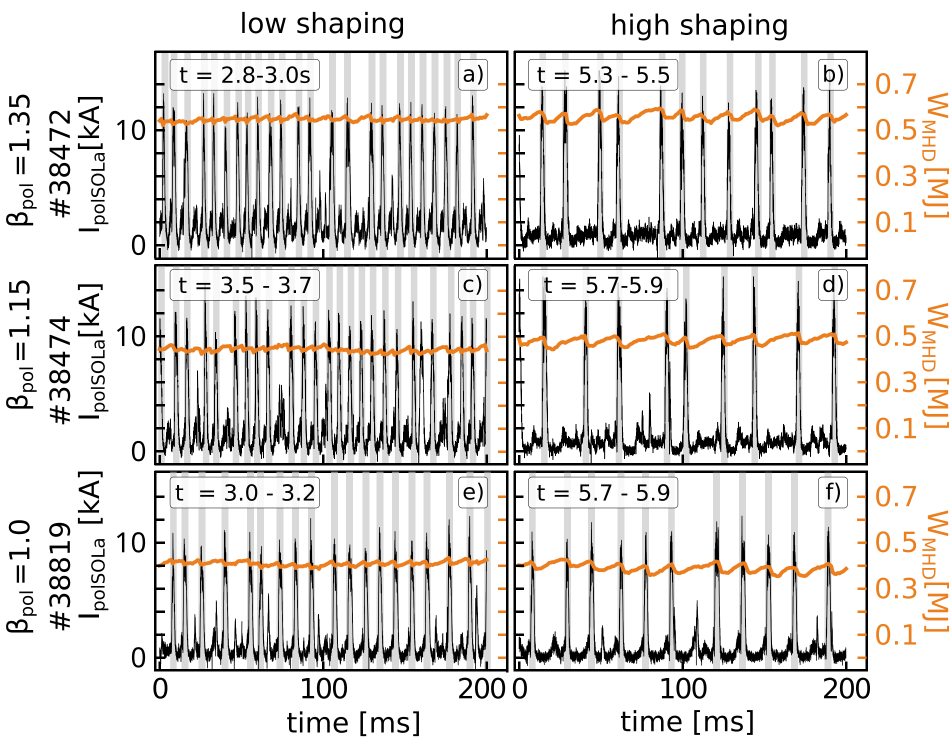

Figure 5. The divertor shunt current I_{polSOLa} is shown for discharge #38472 in panels (*a*) and (*b*), #38474 in (*c*) and (*d*), and #38819 in (*e*) and (*f*). The left panels correspond to the low-shaping phases, while the right panels show the high-shaping phases. The stored MHD energy is also depicted on the right *y*-axis in orange. Additionally, vertical grey stripes indicate the phases that were excluded from the analysis.

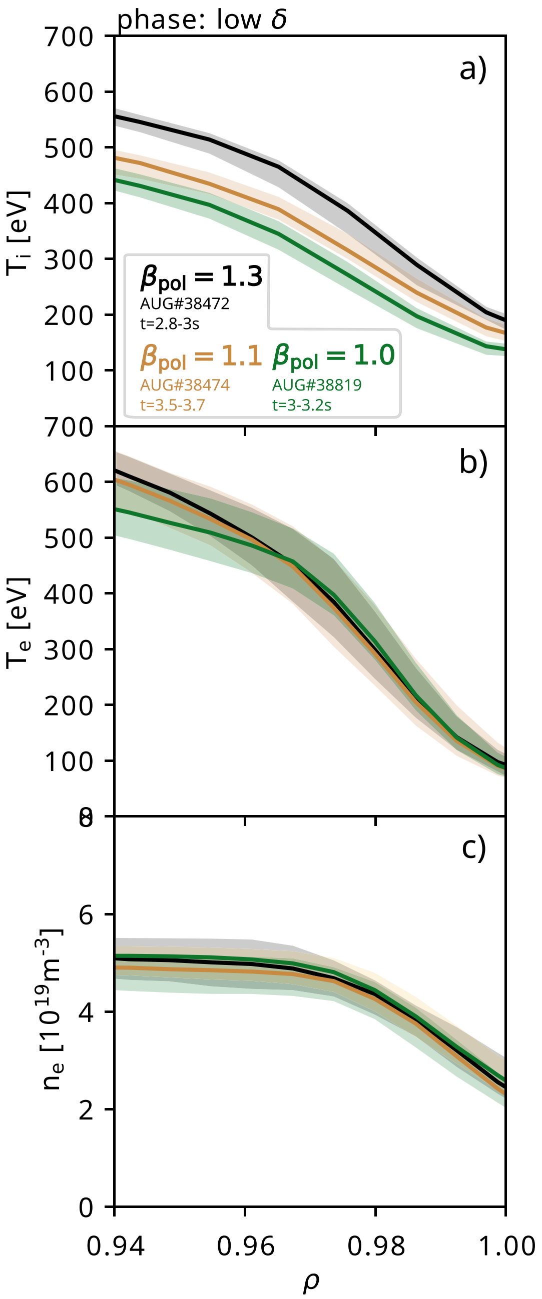

Figure 6. Reconstructed kinetic profiles at different β_{pol} in the low shaping phase at the plasma edge: ion temperature (*a*), electron temperature (*b*) and electron density (*c*). Black lines represent the high β_{pol}, orange lines medium β_{pol} and green low β_{pol}. Lines are showing the medians, the shaded areas are 95% of the temporal variation for the 200 ms time windows.

0.97) for the low β_{pol} discharge. The profile of n_{e} (figure 6(*c*)) does not change within the uncertainty. The ion temperature, however, shows significant increase with β_{pol} both at the pedestal top and at the separatrix. This behaviour is expected because the increase in β_{pol} is experimentally achieved by heating the ions with NBI beams and therefore increasing the total plasma pressure. However, the picture is more complex because β_{pol} is a global quantity that plays distinct roles in core and edge physics. By heating the ions to increase β_{pol} the Shafranov shift is inevitably also increasing, and it therefore changes both local and global MHD stability, allowing for a higher pressure pedestal. Because of the experimental setup, this higher total pressure pedestal is realised with the increase in T_{i}.

In the following, we compare the effect of shaping on the kinetic profiles. To provide a more concise discussion, we focus on the kinetic profiles for the high β_{pol} case, as the profiles for all three β_{pol} values exhibit qualitatively similar behaviour. A comprehensive analysis encompassing all data points will be detailed in section 5.5. Figure 7 shows the low shaping phases in red and high shaping phases in blue. In this scan, there is remarkably almost no difference in T_{i} (figure 7(*a*)), except for a small deviation at the pedestal foot, closest to the separatrix. The difference is however mostly within the uncertainty. It is also noteworthy that the ion temperature does not change, despite a decrease in NBI heating, which happens due to the β_{pol} feedback. This implies a decrease in ion heat flux at the same T_{i}. With the increase in shaping, the electron density (figure 7(*c*)) shows an increase in width and gradient of the pedestal, at the same separatrix density, indicating that there is a process that allows for a reduced particle transport with higher shaping or a particle pinch. The electron temperature (figure 7(*b*)) decreases slightly, which can be explained by the longer ∇T_{e} inter-ELM recovery time [39, 40] and higher $\mathrm{n_e}$ in the high shaping phase. During an ELM-cycle, $\mathrm{n_e}$ and T_{i} pedestals recover more quickly and therefore an MHD limit is possibly reached before the full T_{e} pedestal recovery. Because the high shaping phase has increased n_{e} pedestal, a smaller contribution of the T_{e} pedestal is possible in the later phase. While the ∇T_{e} recovery time accounts for this to an extent, there may be additional underlying causes. The relation between ion and electron heat transport, particle transport, and possible changes in sources is the topic of an ongoing analysis.

In both figures, it is shown that beta and shaping have a different effect on density and temperature of ions and electrons. While the total pressure of the plasma plays an important role, especially in global MHD stability, as can be seen in the following section, the presented examples underline the importance of also treating the pedestals separately.

5. MHD stability

5.1. Global peeling ballooning stability

To assess the global peeling-ballooning stability, the stability boundary is calculated using the code MISHKA and as input the reconstructed equilibria, and the pressure and current profiles. Figure 8(*a*) shows the change in the total pressure profile for the high β_{pol} discharge #38472. As the shaping increases, the total pressure pedestal gets wider and steeper. This would typically cause the bootstrap current to also increase, however, as can be seen in figure 8(*b*), this is not the case. Higher density and lower temperature both contribute to the collisionality increase, which further damps the bootstrap current build-up.

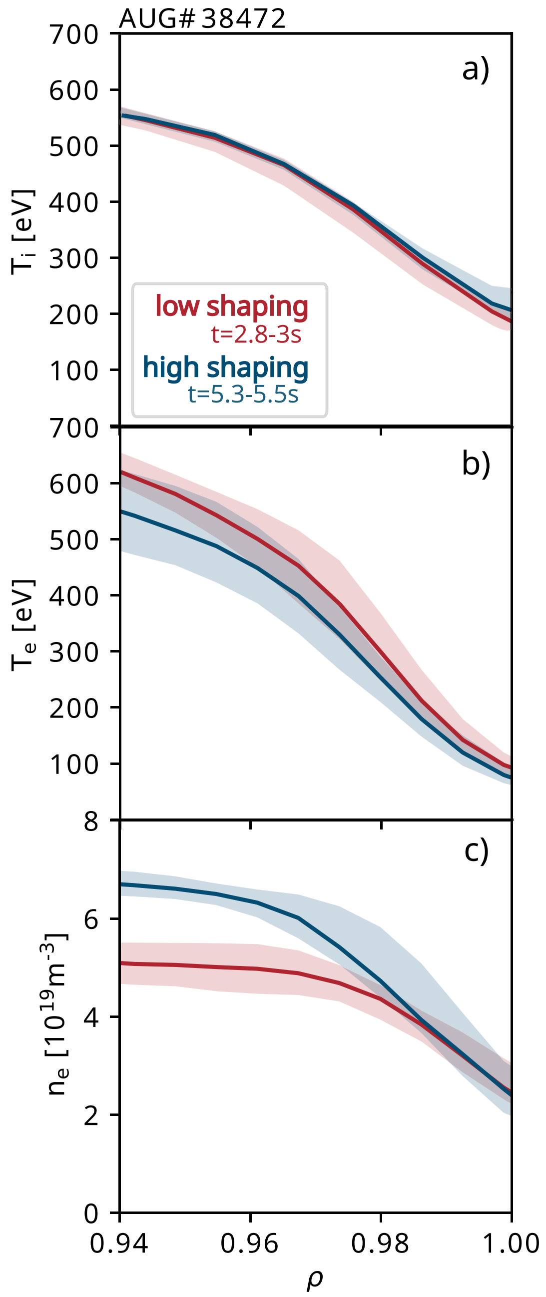

Figure 7. Reconstructed kinetic profiles at different shapes for the high β_{pol} at the plasma edge: ion temperature (*a*), electron temperature (*b*) and electron density (*c*). Red lines represent the low shaping, and blue lines high shaping. Lines are showing the medians, the shaded areas are 95% of the temporal variation for the 200 ms time windows.

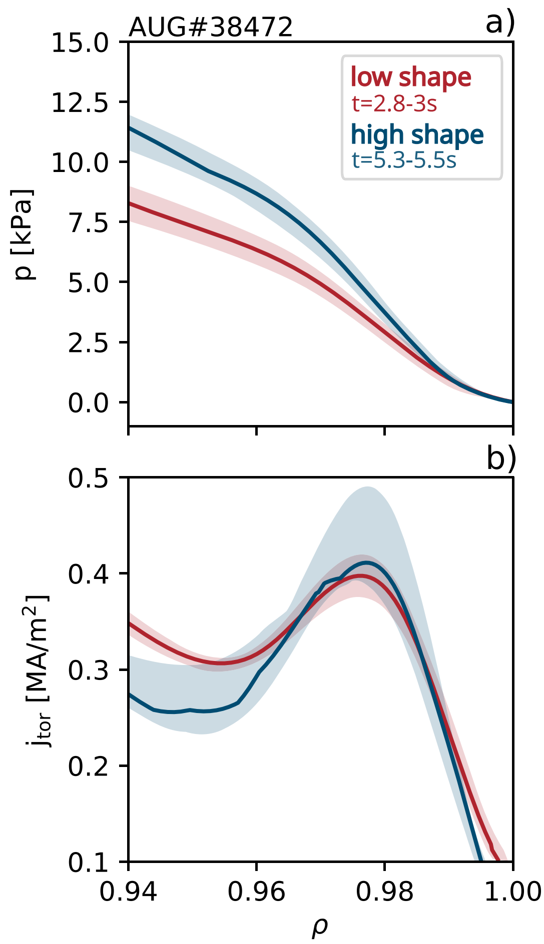

Figure 8. Pressure and current profiles at different shapes for the high β_{pol} case at the plasma edge. Red lines represent the low shaping, and blue lines high shaping. Lines are showing the medians, the shaded areas are 95% of the temporal variation for the 200 ms time windows.

Figure 9 depicts the results of global peeling–ballooning analysis with the code MISHKA as a $j-\alpha$ diagram, with j_{tor} being the flux surface averaged current density and α the normalised pressure gradient. The growth rate $\gamma = 0.04\omega_A$ (4% of Alfvén frequency) of the most unstable mode is taken as the stability limit and shown as a solid line. The operational points are depicted as triangles with the same colour code as in previous figures. As is commonly observed, the global stability analysis shows that increased shaping moves the stability limit towards higher values of normalised pressure gradient α, thereby allowing the total pressure gradient to grow. The toroidal current density, however, does not increase for the reasons previously mentioned.

This further underlines that, particularly in this case, the mode structure that changes the most has rather ballooning than peeling characteristics, since ballooning modes are driven by α. Therefore, we investigate how the local features of ideal $n \to \infty$ ballooning stability develop in different pedestal regions.

5.2. Local ideal ballooning modes

The local IBMs are stabilised by the square of the magnetic shear. The two-dimensional distribution of the local magnetic shear s_{loc}, calculated as defined in [41], is depicted as a two-dimensional map in figure 10, where positive s_{loc} regions are marked in blue and negative regions in green. The thin white contours show the areas with the same s_{loc} value, and particularly between green and blue regions they are marked as thicker white lines where s_{loc} crosses zero. This means that along these zero-crossing lines there is no ballooning mode stabilization. By changing the plasma shape from low shaping

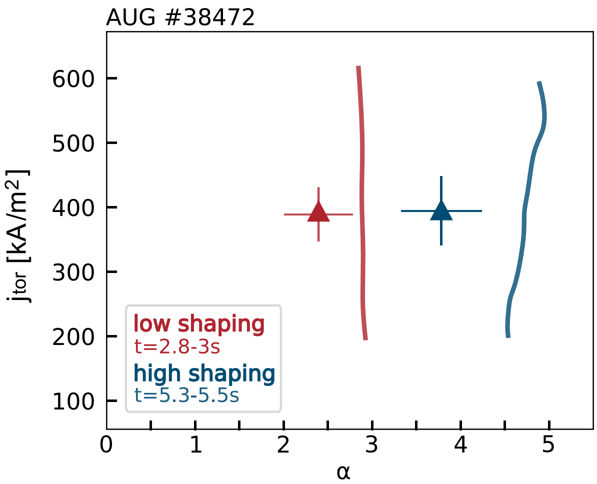

Figure 9. Peeling-ballooning stability for the ELM-filtered time window of high β_{pol} case, shown in toroidal current density j_{tor} and normalised pressure gradient α diagram. Red shows low shaping, and blue high shaping phases. The stability limits are depicted as lines and are representing $\gamma = 0.04\omega_{\mathrm{A}}$. Triangles are mark operational points.

shown in (*a*), to high shaping shown in (*b*), a small region of negative s_{loc} in the upper LFS appears, defining an additional contour of zero shear. Since the stabilising term is $s_{\mathrm{loc}}{}^2$, a negative shear still has a stabilizing effect, even though the global surface averaged shear decreases. Even though this change may not seem significant, due to the localisation of ballooning modes on the LFS it can introduce substantial changes to the distribution of the IBM instability. The drive for the ballooning modes is the normalised pressure gradient α. HELENA takes the experimental α_{exp} from input and also computes the critical α_{crit} at which the plasma would be ballooning unstable. In figure 11(*a*), α_{exp} is shown as full lines and α_{crit} as dashed lines, in red for low shaping and blue for high shaping.

The figure indicates that for higher shaping, as the critical pressure gradient gets higher and wider, and the experimental values follow. However, dashed circles show the regions of the pedestal that are the closest to the ideal ballooning stability limit. In the low shaping time window, this is the case in the maximum gradient region at $\rho \approx 0.975$ and as the shaping increases, two unstable regions appear on the sides of the α_{exp} profile. This can also be observed in figure 11(*b*) where the marginal ballooning stability factor F_{marg}, defined as $F_{\mathrm{marg}} = \alpha_{\mathrm{crit}}/\alpha_{\mathrm{exp}}$ is shown. Here it is observable that for higher triangularity, the stable region in the outer core shifts inward, towards lower values of ρ_{pol}. We compare this F_{marg} minimum location change with the change in electron pressure pedestal width for three different β_{pol} values.

5.3. Effect of plasma boundary and profiles

To partially disentangle the effects of plasma shaping and the pressure and current profiles on the local IBMs, we artificially insert the low (high) shape—profiles into the high (low) shape plasma boundaries and repeat the local ideal ballooning analysis. In figure 12 the first column depicts the actual (*a*) α_{exp} and α_{crit} and (*d*) F_{marg} as compared for high and low shaping.

In the second column, the blue lines show again the actual high shaping case, and the turquoise lines represent the HELENA run where we use the high shaping profiles, however combine them with the low shaping plasma boundary.

In the third column, the opposite is done: the red lines show the original low shaping case, and the orange combines low δ profiles with high shaping plasma boundary. The conclusion following from this test is that the plasma boundary we use linearly increases or decreases the local IBM stability, which can be seen in figures 12(*e*) and (*f*), whereas the profiles influence the actual structure of F_{marg} profile determining if there is a local stability maximum in the pedestal middle or not. One should note that this does not fully disentangle the effect of profiles and equilibrium, since only the plasma boundary is given as an input. This means that the actual equilibrium is reconstructed taking into account the profiles; therefore, the structure of the F_{marg} is mostly determined by the effect of the profiles on the magnetic equilibrium.

In the middle column, it is notable that both high and low triangularity plasma boundaries result in characteristic two F_{marg} minima and a local maximum in the middle of the pedestal. This suggests that the effect of profiles on the equilibrium actually provide the access to the second stability region, which will be discussed in the following section.

5.4. Access to second stability in $\mathrm{s}-\alpha$ diagrams

As mentioned, the stabilizing factor in the ballooning equation is determined by the square of the magnetic shear. Consequently, even if there is a locally negative magnetic shear, its square retains a stabilizing influence. In typical ASDEX Upgrade setups, this occurs predominantly on the LFS, where ballooning modes are destabilized by unfavourable curvature, as can be seen in figure 10(*b*). When the local shear $\mathrm{s}_{\mathrm{loc}}$ changes sign, its square value is zero, resulting in no stabilising effect. This contributes to the local minimum of F_{marg} at both the top and the foot of the pedestal. Additionally, the pressure affects the magnetic shear by amplifying its poloidal variation, primarily because of the intensified Shafranov shift. This enhancement effectively reinforces the stabilizing impact.

The influence of poloidally varying magnetic shear is also evident in the $\mathrm{s}-\alpha$ diagram, as described in [27] section 3.2. In summary, within the plasma edge, enhanced pressure gradients induce a bootstrap current that alters the q profile. This results in a local reversal of the shear, particularly at the LFS where ballooning modes are concentrated. Further increments in α serve to reduce the negative local shear at the LFS even more. This increases the square of the local magnetic shear, therefore the IBM are further stabilized, transitioning the operational point into the second stability region. Consequently, if the pedestal middle resides within the second stable region, it enables the attainment of higher pressure gradients and enhances plasma confinement. In such scenarios, the pressure gradient is not constrained by local IBMs, but rather by global finite-*n* effects.

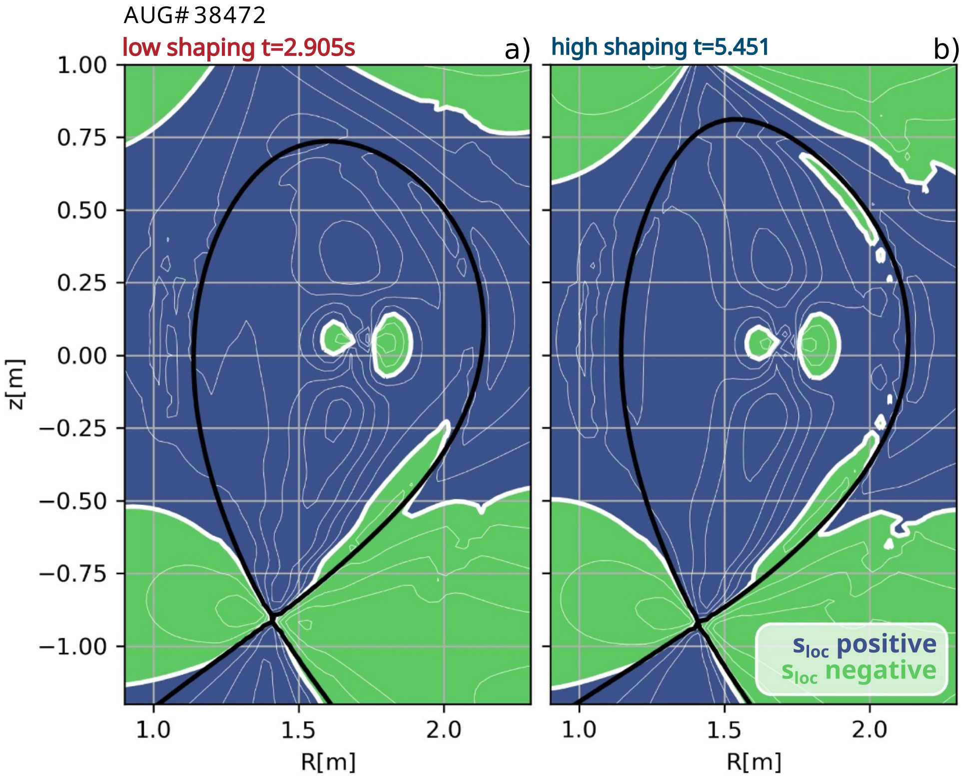

Figure 10. Two-dimensional map of local magnetic shear (s_{loc}) for the low shaping phase shown in (*a*) and high shaping phase shown in (*b*) for discharge #38472: $s_{\mathrm{loc}} > 0$ is marked in blue and $s_{\mathrm{loc}} < 0$ in green. The black line is showing the separatrix, and thin white contours the surfaces on which s_{loc} is constant. The surfaces where $s_{\mathrm{loc}} = 0$ are marked as thick white contour, and in these regions there is therefore no ballooning mode stabilisation.

The relation of the first and the second stability regions is shown in figure 13 where the diagrams are depicted for the high β_{pol} discharge #38472. In figure 13(*a*) the unstable region and the first and second stable regions are sketched in gray. The three columns are showing three different radial positions in the pedestal; left column showing $\rho_{\mathrm{pol}} = 0.965$ (the F_{marg} minimum in high triangularity pedestal top), middle column $\rho_{\mathrm{pol}} = 0.975$ (the F_{marg} minimum in low triangularity pedestal middle) and $\rho_{\mathrm{pol}} = 0.985$ (the F_{marg} minimum in high triangularity pedestal foot). The first row depicts the low triangularity phase and the second row the high triangularity phase.

Each panel shows where the operational point, marked as a triangle, is located in the $\mathrm{s}-\alpha$ space. The profiles of current and pressure gradient used as input for HELENA are then scaled from 80% to 120% of their initial value. The resulting grid is in figure 13 represented as dots. Together with the original plasma boundary, the equilibrium is reconstructed for each point and the local IBM stability is evaluated. To each point on the grid, a value of F_{marg} is attributed, and represented as the colour map where blue regions are stable and red unstable. The distance of the operational point to the stability limit, shown as a black contour line, indicates how ballooning unstable the given configuration is. One should note that while local IBMs are a proxy for KBMs, which are qualitatively very similar, KBMs tend to be less stable. Therefore, points in the white shade could already be susceptible to KBM instabilities.

In the first row, where the low triangularity case is shown, the stability limit stays at relatively low values of s and α at all three locations. At $\rho_{\mathrm{pol}} = 0.965$ (figure 13(*a*)) the operational point is deep in the first stability region, and higher values of the pressure gradient are therefore unattainable. Deeper in the pedestal region, at $\rho_{\mathrm{pol}} = 0.975$ (figure 13(*b*)), the operational point moves slightly towards the transition region, however at $\rho_{\mathrm{pol}} = 0.985$ (figure 13(*c*)) it is back in the first stability at low pressure gradient values.

The second row shows the high triangularity case: Already at $\rho_{\mathrm{pol}} = 0.965$ (figure 13(*d*)), at the top of the $\mathrm{p_e}$ pedestal, the operational point is closer to the transition to the second stability. In panel (*e*) it is evident that the operational point has access to second stability, partially because of the higher α, however also the stability boundary is at significantly higher values of magnetic shear, which can be attributed to the different plasma shape compared to the first phase. At the pedestal foot, in panel (*f*) the stability limit is even higher and the operational point is in the transition region.

For F_{marg} profiles in figure 11, this can be interpreted as follows: for the high shaping case, in the region of increased stability, that is for $0.965 < \rho_{\mathrm{pol}} < 0.985$, the value of F_{marg} is close to 1. However, because this region is second stable,

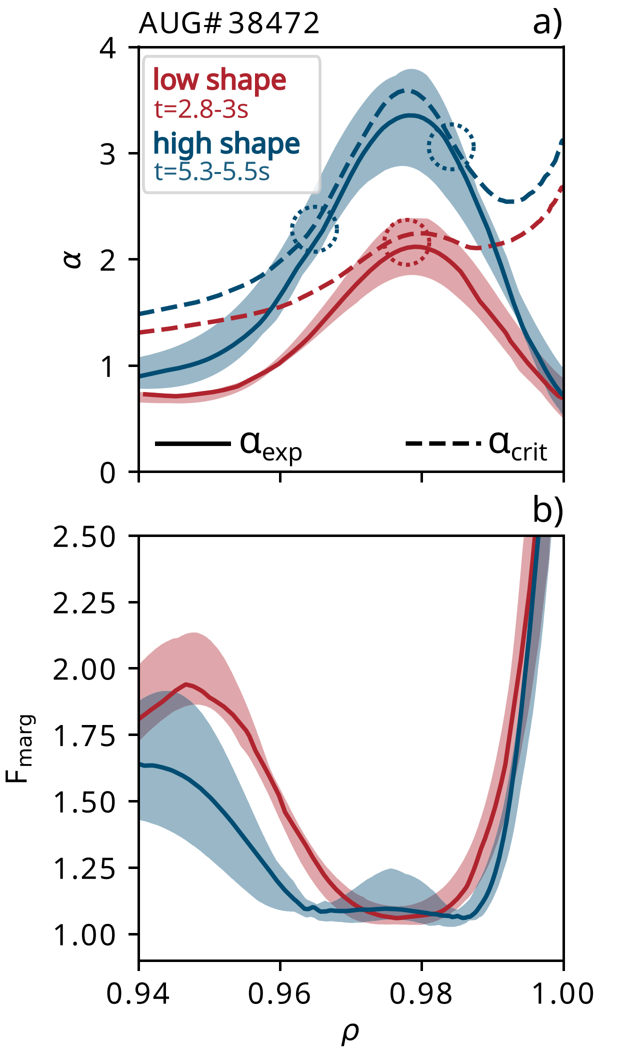

Figure 11. Radial profiles of critical α (dashed line) and experimental α (full line) in (*a*) and ballooning stability factor F_{marg} in (*b*). Red shows low shaping, and blue high shaping phases. The full line represents the temporal median, and the shaded area the 95% of the temporal variation for the analysed 100 ms.

the pressure gradient is not actually limited by the IBM, since increasing α_{exp} only stabilizes the IBMs as can be seen in figure 13(*e*). Furthermore, if α_{exp} in figure 11(*a*) were to increase, the values of α_{crit} would increase at a higher rate. This information can only be extracted using the $s-\alpha$ diagram analysis described above, and would be impossible to get looking at profiles only.

5.5. Comparison of the electron, ion and total pressure profiles with F_{marg} and ∇E_r

The radial positions of the electron and ion pedestal tops are compared with F_{marg} and the gradient of E_r, normalised to c_s/R, with c_s being the sound speed calculated as $c_s = \sqrt{T_e + T_i/m_i}$ and used as a proxy for the $E \times B$ shear. The pedestal top position is set by fitting one line through the region of maximal gradient, and one line through the outer core, and determining the radial position at which these two lines cross, similarly as described in [42].

In figure 14, it is shown that the p_e pedestal (first row) strongly correlates with F_{marg} (second row) since the value of F_{marg} lies between 1.2 and 1.25 at the radial position of the respective p_e pedestal top. It is also shown that similarly, p_i (third row) correlates with ∇E_r (fourth row). We illustrate this for the range of β_{pol} values, high in the first, medium in the second and low in the third column. The pedestal tops of p_e and p_i are marked with dashed red and blue lines for high and low triangularity, and then projected to the rows below, showing F_{marg} and ∇E_r, respectively.

Inspecting the electron pressure profiles (figures 14(*a*)–(*c*)) it is notable that only #38474 has a pressure gradient that slightly increases in the high shaping phase. In the other two cases, the gradient stays the same, while the pedestal gets wider and higher. Pedestal widening with the increased shape dominantly comes from the widening of density profiles, where electron temperature decreases and results in a constant p_e gradient, as can be seen in figure 7. The positions of the pedestal top are projected to F_{marg}, and the standard deviation of F_{marg} is only 0.02, around the median value $F_{marg} = 1.21$. In figures 14(*d*)–(*f*), this region is marked with the gray stripe. It is important to note that HELENA, the code used to calculate ballooning stability factor F_{marg}, has no information about E_r.

In comparison with the F_{marg} profiles in figures 14(*d*)–(*f*), it is evident that the profile shifts to higher values as β_{pol} increases. Furthermore, the peak in the pedestal centre during the high-shaping phases becomes more pronounced, driven by the shift of the stability boundary towards higher values of s and α, as detailed in section 5.4.

The particularly strong correlation between p_i (figures 14(*g*)–(*i*)) and ∇E_r (figures 14(*j*)–(*l*)) partially comes from the fact that in the pedestal, E_r, calculated as defined in equation (1), is dominated by the diamagnetic term of main ions, which is directly proportional to ∇p_i. However, the turbulent processes dominating the radial transport of particles and ion heat are suppressed by ∇E_r. This self-sustaining mechanism is however also limited by the neoclassical transport and MHD.

To further examine the correlations between the given quantities, we perform the following analysis: for each pressure profile p_e, p_i and total pressure p the radial position of the pedestal top is determined. Then, a value of F_{marg} and ∇E_r at this particular radial position is evaluated and a median ($\overline{F_{marg}}$ and $\overline{\nabla E_r}$) for the 6 points (three β_{pol} and two shapes each) is calculated. The values of the medians and the respective standard deviations are listed in table 2. In figure 15 the radial positions of the pedestal tops are plotted on the x axes and the radial positions of $\overline{F_{marg}}$ and $\overline{\nabla E_r}$ are plotted on the y axes. The error bars are showing the range of the standard deviation. A diagonal $x = y$ gray line is plotted in each panel. The strength of correlation is also quantified as R^2 value and listed in table 2.

As can also be seen in figures 14(*a*)–(*f*), there is a strong correlation between the p_e pedestal top position F_{marg} value of 1.21. This can also be seen in figure 15(*a*) that shows correlations with the positions of $\overline{F_{marg}}$. Small error bars indicate

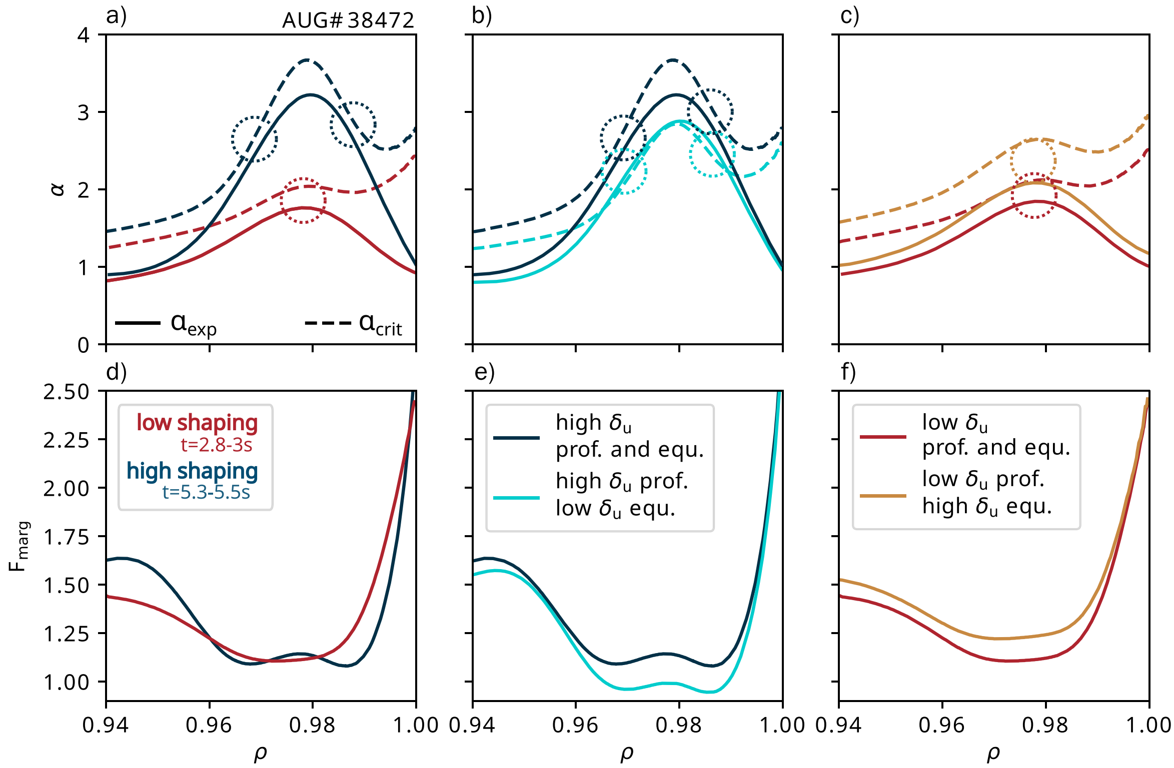

Figure 12. Radial profiles of critical α (dashed line) and experimental α (full line) in (*a*)–(*c*) and ballooning stability factor $F_{\mathrm{marg}} = \alpha_{\mathrm{crit}}/\alpha_{\mathrm{exp}}$ in (*d*)–(*f*) at two distinct time points. The actual high and low shaping values are shown in (*a*) and (*d*), where red marks low shaping, and blue high shaping phases. In (*b*) and (*e*) in blue the actual values are also shown, and in turquoise high shaping profile is mixed with low shaping plasma boundary. In (*c*) and (*f*) the opposite is done: the original low shape phase in red, is compared with high shaped plasma boundary mixed with the original low shape phase profiles in orange. Dashed circles mark the regions where α_{exp} and α_{crit} are the closest.

small standard deviations around the median. The exception to small error bars is discharge #38474 in the low triangularity phase, which, as can be seen in figure 11(*e*) has a particularly flat profile, exactly in the region of expected F_{marg} value.

The ion pressure pedestal top, shown in figure 15(*b*), has significantly larger error bars, due to the larger scatter of F_{marg} values at the pedestal top positions. In the total pressure positions in figure 15(*c*), the general trend is still observable, however with larger variations.

Figure 15(*d*) shows the correlation between p_{e} pedestal top and position of the median of $\overline{\nabla E_r}$, where all the triangles, representing the high-shaped phases, are wider than the median, and all circles, representing the low-shaped phases, are narrower than the median. The positions of p_{e} pedestal tops for low and high triangularity are at two distinctly different values of $\overline{\nabla E_r}$, which indicates additional stabilisation in the high triangularity cases.

The strongest correlation with E_{r} is found in p_{i} shown in figure 15(*e*), where despite smaller changes in the pedestal width, the pedestal top positions align well with the position of $\overline{\nabla E_r}$ and the error bars are small. Figure 15(*f*) reflects these correlations as well, albeit with slightly larger deviations from $\overline{\nabla E_r}$.

6. Discussion and conclusions

In this study, we analysed the impact of various physical mechanisms on the pedestal width, particularly focusing on the effects of shaping and normalised poloidal pressure in ASDEX Upgrade. We investigated how these factors influence temperature and density, as well as how they affect electrons and ions separately.

All analysed discharges are in ELMy H-mode, so the overall limit on the total pressure pedestal is set by the global MHD peeling ballooning modes. It is generally observed, that with the change in shape, the peeling ballooning stability limit moves towards higher values of the normalised pressure gradient α and current density j. In the presented discharges, due to their closeness to the ballooning boundary, only the increase in alpha can be directly observed from the scan. It was found that alpha also plays a more important role, due to the fact that temperature and density change differently with increased shaping, both increasing collisionality which lowers the bootstrap current, while increased total pressure gradient enhances it, so maximal j_{tor} stays approximately the same.

Notable differences between the influence of shaping and β_{pol} are observed. It is shown that β_{pol} had no influence on

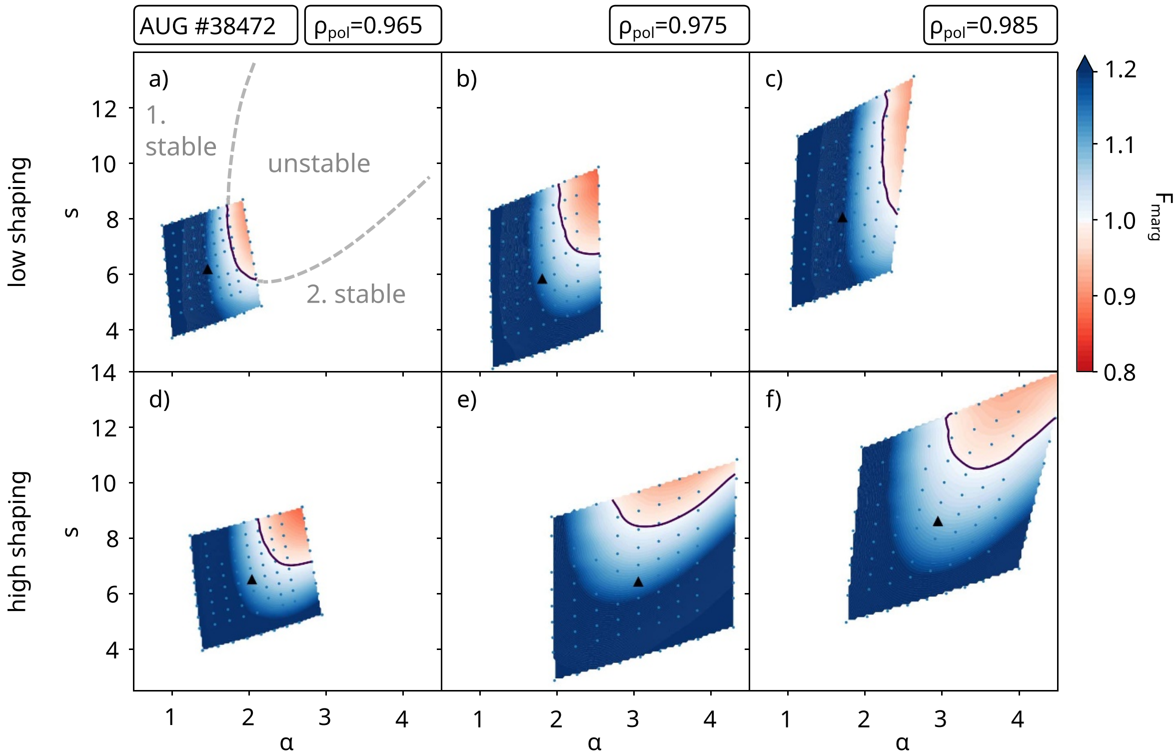

Figure 13. $s-\alpha$ diagrams for 3 different positions in the pedestal at low shaping in the first row (*a*)–(*c*) and high shaping in the second row (*d*)–(*f*) for discharge #38472. Blue contours represent marginally ballooning stable regions and red marginally ballooning unstable regions, the full line is the ballooning stability limit where $F_{\mathrm{marg}} = 1$. Operational points are marked with black triangles.

density, a small influence on electron temperature, and a substantial influence on ion temperature—partially because of the functionality of the β_{pol} feedback loop. Shaping most significantly influences the density profile, with its width and gradient increasing. The electron temperature is somewhat affected, and it is lower in higher density phases. Since electron temperature is shown to recover more slowly in an inter-ELM cycle [39], this can be interpreted as a rise in temperature during the ELM cycle, however only until a certain resulting electron pressure gradient is reached, which stays clamped at a constant value. The ion temperature does not change significantly with shaping, however, in the high shape phases, β_{pol} feedback causes decreased NBI heating and the plasma volume is larger. Both effects imply lower ion temperature, so it is inevitable that there is a decrease in heat flux.

One reason for the changes observed with shaping is the alteration of the local magnetic shear (s_{loc}), that creates a region with strong but negative magnetic shear, which stabilises local IBMs. This causes transitions from having one unstable region, covering most of the pedestal, to the pedestal top and foot being unstable. The middle of the pedestal then enters the second stability region where no ballooning modes occur, making pedestal widening possible. This is also reflected in substantial correlation between the pedestal top position of the electron pressure p_{e} and a certain value of the ballooning stability factor F_{marg}. A correlation was also found between pedestal top position of the ion pressure p_{i} and a certain value of the gradient of the radial electric field ∇E_{r}. The resulting total pressure widths have a weaker, but still observable correlation with both median of F_{marg} and ∇E_{r}.

A possible picture, analysing this correlation coming from the plasma core, emerges: in the core the transport is dominated by turbulence. Approaching the pedestal, ∇E_{r} reduces turbulence strongly, however the reduction changes as ∇E_{r} varies over the pedestal region. At a certain threshold of ideal ballooning stability, the local E_{r} stabilisation is not strong enough and local IBMs (here IBMs can be replaced by KBMs or resistive ballooning modes) occur, enhancing the transport. After this region, the E_{r} stabilisation increases and together with other modes, the IBMs are reduced again. Note that in the case of high triangularity, even though F_{marg} is close to the ballooning stability in the pedestal middle, as explained in section 5.3, the pressure gradient is rather stabilizing the IBMs, and not limited by them, due to the second stability access.

The total pressure is foremost constrained by global MHD phenomena, and it sets the overall limit on the pedestal structure, within which the individual effects of transport, turbulence and its reduction put further limits on the pedestal shape. The interplay between shaping and β_{pol} significantly affects the pedestal structure. Shaping predominantly influences density and electron temperature, while β_{pol} impacts the position of MHD stability limits and therefore the overall width of the pedestal. The identified physical processes that enhance the pedestal and reduce radial transport are $E \times B$ shear and magnetic shear. These stabilizing factors are counteracted foremost by the global MHD stability limit, which, when crossed,

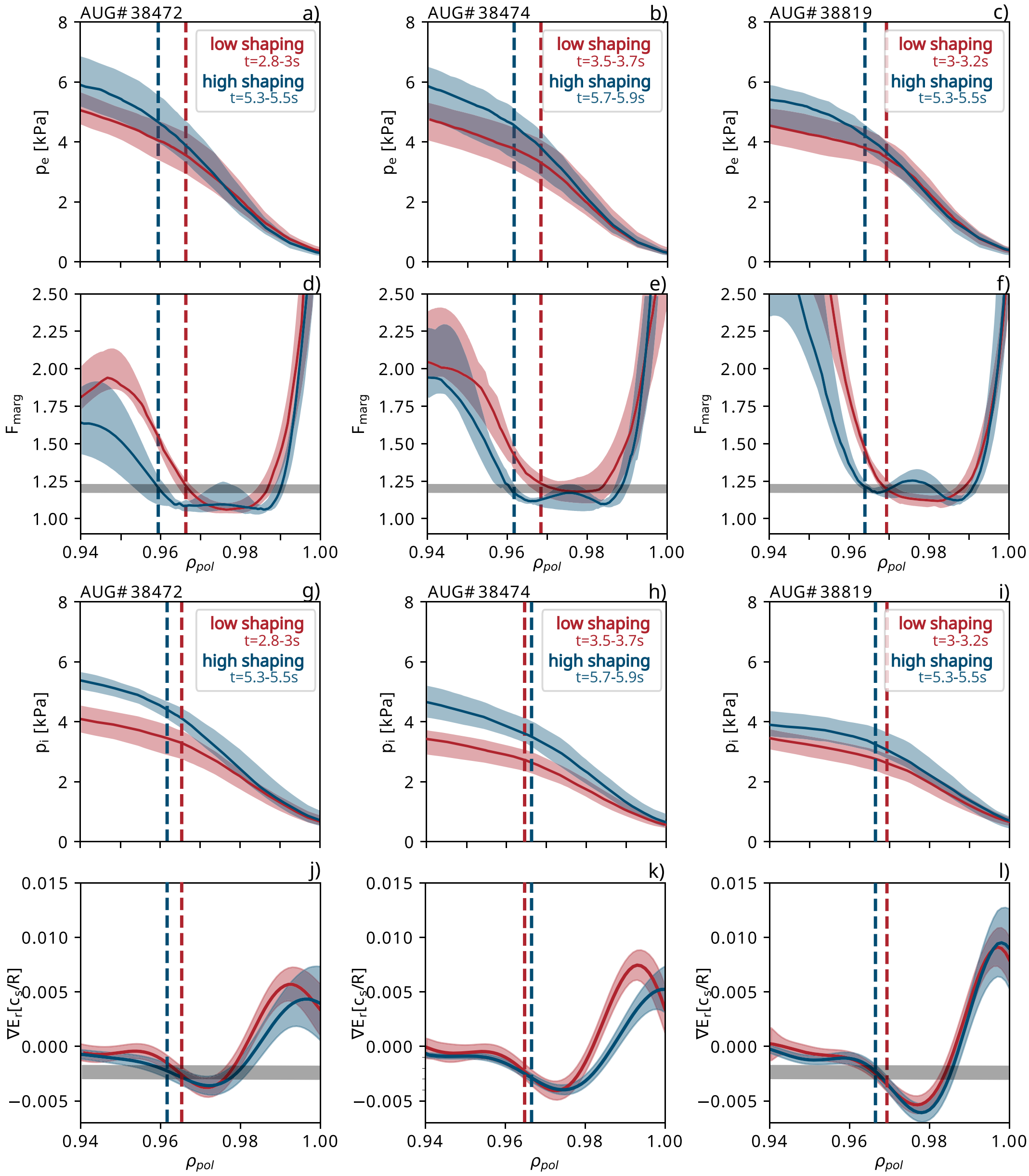

Figure 14. Profiles of electron pressure p_e in the first row (*a*)–(*c*), F_{marg} in the second row (*d*)–(*f*), ion pressure p_i in the third row (*g*)–(*i*) and gradient of radial electric field ∇E_r normalised to the sound speed c_s and major radius R in the fourth row (*j*)–(*l*). Full lines are showing the median and shaded areas the 95% of the temporal variation for the analysed 200 ms. Red is marking the low shaping and blue the high shaping phases. Pedestal tops are determined using a two line fit through maximum gradient and outer core and marked with vertical dashed lines, the horizontal gray stripe in panels in the second row (*d*)–(*f*) and the fourth row (*j*)–(*l*) shows the standard deviation around the median value of F_{marg} and ∇E_r values at the pedestal top of p_e and p_i, respectively.

causes an ELM and therefore a pedestal crash. Furthermore, local IBMs exist in different pedestal regions where they cause additional transport.

These results demonstrate that even though scaling laws and empirical models are useful, they cannot fully predict pedestal behaviour in future machines. Separately treating ion and electron pedestals for temperature and particles is essential for understanding the pedestal structure. Our analysis indicates that magnetic shear significantly influences the electron pressure profile, whereas the ion temperature remains unaffected by shear but correlates with E_r. It is suggested that distinct mechanisms must be considered for different pedestal components when evaluating future machines, such as ITER. This raises the need for further testing of this hypothesis and integrating these mechanisms into models capable of performing predictive calculations.

Several open questions remain, such as the behaviour of ion and electron heat diffusivities and the presence of other microturbulent modes in the pedestal, which are subjects of ongoing research. Additionally, the role of resistivity needs further investigation, either through resistive codes or by examining the response of ballooning modes under varying

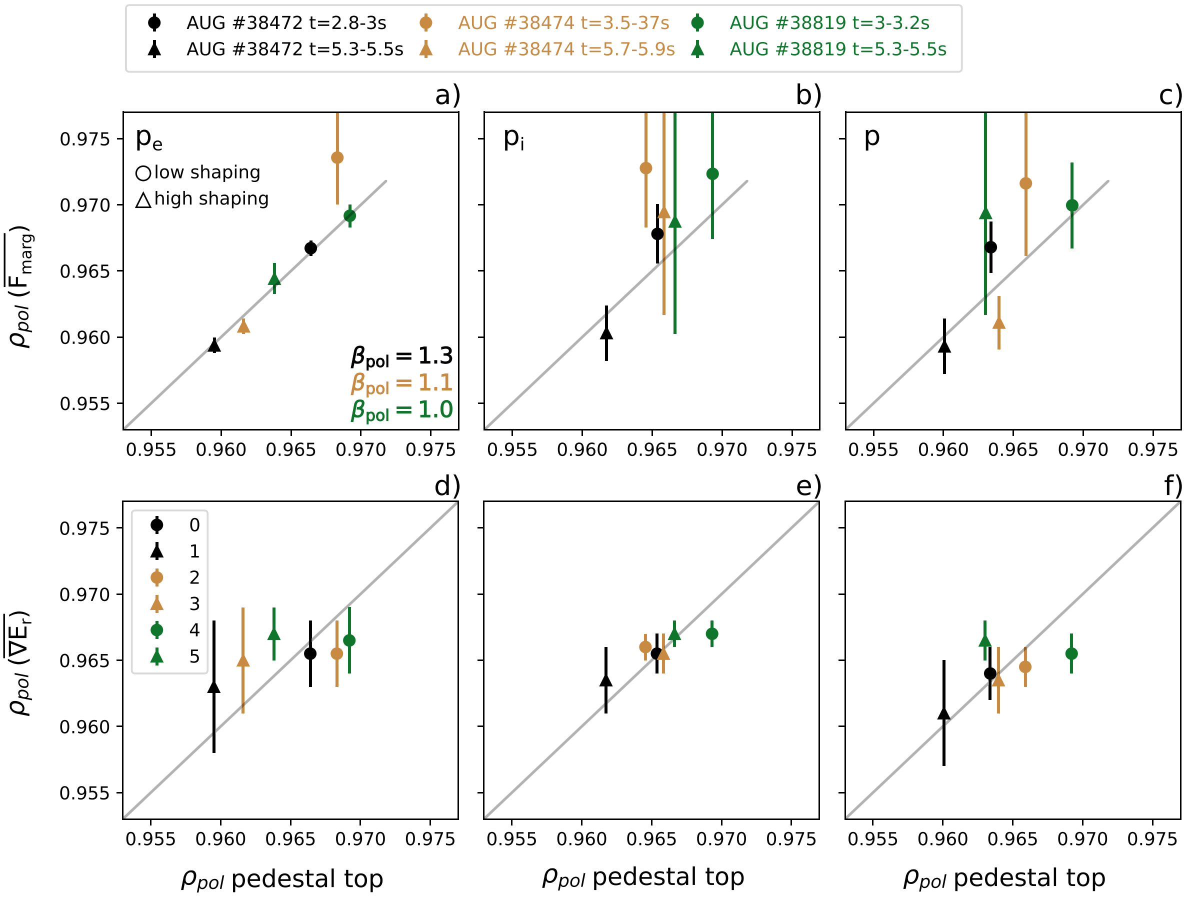

Figure 15. Correlations between radial positions of the pedestal top in electron, ion and total pressure (p_e in (*a*) and (*d*), p_i in (*b*) and (*e*), and p in (*c*) and (*f*)) with the radial position of the median values $\overline{F_{marg}}$ in the first row and $\overline{\nabla E_r}$ in the second row. Circles mark the low shaping phases and triangles the high shaping phases. The value of β_{pol} is indicated in colours, $\beta_{pol} = 1.3$ in black, $\beta_{pol} = 1.1$ in orange, and $\beta_{pol} = 1.0$ in green. The error bars are showing the range of ρ_{pol} that is in the standard deviation.

Table 2. Median values and standard deviation values of ∇E_r and F_{marg} and R^2 value, quantifying correlation between their radial positions and pedestal top positions.

	$\overline{\nabla E_r}$ [c_s/R]	$\sigma(\overline{\nabla E_r})$	$R^2(\overline{\nabla E_r})$	$\overline{F_{marg}}$	$\sigma(\overline{F_{marg}})$	$R^2(\overline{F_{marg}})$
p_e	−0.002 55	0.000 85	0.85	1.21	0.02	0.95
p_i	−0.002 62	0.000 49	0.86	1.18	0.07	0.79
p	−0.002 27	0.000 67	0.8	1.21	0.07	0.84

collisionalities. While this study highlights the critical role of magnetic shear in pedestal formation, an unresolved question is how these modes interact with $E \times B$ shear, as this effect is not accounted for in HELENA.

It is important to note that in distinct pedestal regions, the stabilisation and drives of different modes have varying strengths. Therefore, a simple model for the entire pedestal can never be accurate. Instead, the detailed physics in the pedestal must be well resolved radially. This is challenging both from experimental and modelling point of view, especially when considering different electron and ion channels of particle and heat transport, however necessary to explain the varying pedestal behaviours.

Acknowledgments

Lidija Radovanovic is a fellow of the Friedrich Schiedel Foundation for Energy Technology. This work has been carried out within the framework of the EUROfusion Consortium, funded by the European Union via the Euratom Research and Training Programme (Grant Agreement No. 101052200—EUROfusion). Views and opinions expressed are however those of the author(s) only and do not necessarily reflect those of the European Union or the European Commission. Neither the European Union nor the European Commission can be held responsible for them. The authors acknowledge TU Wien Bibliothek for financial support through its Open Access Funding Programme.

ORCID iDs

L. Radovanovic https://orcid.org/0000-0002-1311-0482
E. Wolfrum https://orcid.org/0000-0002-6645-6882
M.G. Dunne https://orcid.org/0000-0002-5259-9970
G.F. Harrer https://orcid.org/0000-0002-1150-3987
F. Aumayr https://orcid.org/0000-0002-9788-0934

References

[1] Wagner F. *et al* 1982 Regime of improved confinement and high beta in neutral-beam-heated divertor discharges of the ASDEX tokamak *Phys. Rev. Lett.* **49** 1408–12

[2] Biglari H., Diamond P.H. and Terry P.W. 1990 Influence of sheared poloidal rotation on edge turbulence *Phys. Fluids B* **2** 1–4

[3] Maggi C.F. *et al* (EFDA-JET Contributors for the Pedestal, Edge Physics and the Steady State Operation Topical Groups of the ITPA) 2007 Characteristics of the H-mode pedestal in improved confinement scenarios in ASDEX Upgrade, DIII-D, JET and JT-60U *Nucl. Fusion* **47** 535

[4] Beurskens M.N.A. *et al* (The DIII-D Team, The ASDEX Upgrade Team and JET-EFDA Contributors) 2011 H-mode pedestal scaling in DIII-D, ASDEX Upgrade and JET *Phys. Plasmas* **18** 056120

[5] Leonard A.W., Groebner R.J., Osborne T.H. and Snyder P.B. 2008 Influence of global beta, shape and rotation on the H-mode pedestal structure in DIII-D *Phys. Plasmas* **15** 056114

[6] Snyder P.B., Groebner R.J., Hughes J.W., Osborne T.H., Beurskens M., Leonard A.W., Wilson H.R. and Xu X.Q. 2011 A first-principles predictive model of the pedestal height and width: development, testing and ITER optimization with the EPED model *Nucl. Fusion* **51** 103016

[7] Dunne M.G. *et al* (The EUROfusion MST1 Team and The ASDEX Upgrade Team) 2016 Global performance enhancements via pedestal optimisation on ASDEX Upgrade *Plasma Phys. Control. Fusion* **59** 025010

[8] Suttrop W., Gruber O., Kurzan B., Murmann H.D., Neuhauser J., Schweinzer J., Stober J. and Treutterer W. (The ASDEX Upgrade Team) 2000 Effect of plasma shape variation on ELMs and H-mode pedestal properties in ASDEX Upgrade *Plasma Phys. Control. Fusion* **42** A97

[9] Kim S.K., Na Y.-S., Saarelma S. and Kwon O. 2017 Dependence of pedestal properties on plasma parameters *Nucl. Fusion* **58** 016036

[10] Osborne T.H. *et al* 2000 The effect of plasma shape on H-mode pedestal characteristics on DIII-D *Plasma Phys. Control. Fusion* **42** A175

[11] Snyder P.B. *et al* 2009 Pedestal stability comparison and ITER pedestal prediction *Nucl. Fusion* **49** 085035

[12] Luda T. *et al* The ASDEX Upgrade Team and The EUROfusion MST1 Team) 2020 Integrated modeling of ASDEX Upgrade plasmas combining core, pedestal and scrape-off layer physics *Nucl. Fusion* **60** 036023

[13] Luda T., Angioni C., Dunne M.G., Fable E., Kallenbach A., Bonanomi N., Lunt T., Schneider P.A., Siccinio M. and Tardini G. (The ASDEX Upgrade Team and The EUROfusion MST1 Team) 2021 Validation of a full-plasma integrated modeling approach on ASDEX Upgrade *Nucl. Fusion* **61** 126048

[14] Zohm H. 1996 Edge localized modes (ELMs) *Plasma Phys. Control. Fusion* **38** 105

[15] Viezzer E. 2018 Access and sustainment of naturally ELM-free and small-ELM regimes *Nucl. Fusion* **58** 115002

[16] Schneider P.A., Wolfrum E., Groebner R.J., Osborne T.H., Beurskens M.N.A., Dunne M.G., Kurzan B., Pütterich T. and Viezzer E. (The ASDEX Upgrade Team, The DIII-D Team and JET EFDA Contributors) 2013 Analysis of temperature and density pedestal gradients in AUG, DIII-D and JET *Nucl. Fusion* **53** 073039

[17] Urano H. 2014 Pedestal structure in H-mode plasmas *Nucl. Fusion* **54** 116001

[18] Wilks T.M. *et al* 2021 Impact of shape on pedestal characteristics in the wide pedestal quiescent H-mode in the DIII-D tokamak *Nucl. Fusion* **61** 036032

[19] Bowman C. *et al* (JET Contributors) 2017 Pedestal evolution physics in low triangularity JET tokamak discharges with ITER-like wall *Nucl. Fusion* **58** 016021

[20] Frassinetti L. *et al* (JET Contributors) 2020 Pedestal structure, stability and scalings in JET-ILW: The EUROfusion JET-ILW pedestal database *Nucl. Fusion* **61** 016001

[21] Kamada Y., Oyama N., Ide S., Sakamoto Y., Isayama A., Fujita T., Urano H., Suzuki T. and Yoshida M. 2006 Impact of the edge pedestal characteristics on the integrated performance in advanced tokamak operation modes in JT-60U *Plasma Phys. Control. Fusion* **48** A419

[22] Urano H., Aiba N., Kamiya K. and Kamada Y. (The JT-60 Team) 2015 Dependence of pedestal structure on collisionality at fixed beta in JT-60U *Nucl. Fusion* **56** 016005

[23] Groebner R.J. *et al* 2005 Pedestal studies in DIII-D *Fusion Sci. Technol.* **48** 1011–20

[24] Maggi C.F. *et al* (JET Contributors) 2015 Pedestal confinement and stability in JET-ILW ELMy H-modes *Nucl. Fusion* **55** 113031

[25] Horvath L. *et al* (JET Contributors) 2023 Pedestal particle balance studies in JET-ILW H-mode plasmas *Plasma Phys. Control. Fusion* **65** 044003

[26] Dickinson D., Saarelma S., Scannell R., Kirk A., Roach C.M. and Wilson H.R. 2011 Towards the construction of a model to describe the inter-ELM evolution of the pedestal on MAST *Plasma Phys. Control. Fusion* **53** 115010

[27] Radovanovic L., Dunne M., Wolfrum E., Harrer G., Faitsch M., Fischer R. and Aumayr F. (The ASDEX Upgrade Team and The EUROfusion MST1 Team) 2022 Developing a physics understanding of the quasi-continuous exhaust regime: pedestal profile and ballooning stability analysis *Nucl. Fusion* **62** 086004

[28] Harrer G.F. *et al* (The ASDEX Upgrade Team and The EUROfusion MST1 Team) 2022 Quasicontinuous exhaust scenario for a fusion reactor: the renaissance of small edge localized modes *Phys. Rev. Lett.* **129** 165001

[29] Mlynek A., Schramm G., Eixenberger H., Sips G., McCormick K., Zilker M., Behler K. and Eheberg J. (ASDEX Upgrade Team) 2010 Design of a digital multiradian phase detector and its application in fusion plasma interferometry *Rev. Sci. Instrum.* **81** 033507

[30] Kurzan B., Murmann H. and Salzmann H. (ASDEX Upgrade Team) 2001 Improvements in the evaluation of Thomson scattering data on ASDEX Upgrade *Rev. Sci. Instrum.* **72** 1111–4

[31] Hartfuss H.J., Geist T. and Hirsch M. 1997 Heterodyne methods in millimetre wave plasma diagnostics with applications to ECE, interferometry and reflectometry *Plasma Phys. Control. Fusion* **39** 1693

[32] Puetterich T. 2008 Fast CXRS-measurements in the edge barrier of ASDEX Upgrade *35th EPS Conf. on Plasma Physics* (*Hersonissos, 9–13 June 2008*) vol 32D P-2.083

[33] Viezzer E. et al (The ASDEX Upgrade Team) 2013 High-accuracy characterization of the edge radial electric field at ASDEX Upgrade *Nucl. Fusion* **53** 053005

[34] Fischer R., Fuchs C.J., Kurzan B., Suttrop W. and Wolfrum E. 2010 Integrated data analysis of profile diagnostics at ASDEX Upgrade *Fusion Sci. Technol.* **58** 675–84

[35] Fischer R. *et al* 2016 Coupling of the flux diffusion equation with the equilibrium reconstruction at ASDEX Upgrade *Fusion Sci. Technol.* **69** 526–36

[36] Huysmans G.T.A., Goedbloed J.P. and Poedts H. 1991 External resistive modes and toroidicity induced Alfven eigenmodes in tokamaks *Proc. CP90 Int. Conf. on Comp. Phys. Proc.* (*Singapore*) p 371

[37] Galvão R.M.O. and Rem J. 1981 Application of the Suydam method to the balloonings stability problem *Comput. Phys. Commun.* **22** 399–402

[38] Huysmans G.T.A., Sharapov S.E., Mikhailovskii A.B. and Kerner W. 2001 Modeling of diamagnetic stabilization of ideal magnetohydrodynamic instabilities associated with the transport barrier *Phys. Plasmas* **8** 4292–305

[39] Laggner F.M., Wolfrum E., Cavedon M., Dunne M.G., Birkenmeier G., Fischer R., Willensdorfer M. and Aumayr F. (The EUROfusion MST1 Team and The ASDEX Upgrade Team) 2018 Plasma shaping and its impact on the pedestal of ASDEX Upgrade: edge stability and inter-ELM dynamics at varied triangularity *Nucl. Fusion* **58** 046008

[40] Viezzer E. *et al* (The ASDEX Upgrade Team) 2020 Dynamics of the pedestal transport during edge localized mode cycles at ASDEX Upgrade *Plasma Phys. Control. Fusion* **62** 024009

[41] Carthy P.J.M. (The ASDEX Upgrade Team) 2013 Practical expressions for local magnetic shear, normal and geodesic curvatures in an axisymmetric plasma equilibrium of arbitrary cross-section *Plasma Phys. Control. Fusion* **55** 085011

[42] Schneider P.A. *et al* (The ASDEX Upgrade Team, The DIII-D Team and JET EFDA Contributors) 2012 Differences in the H-mode pedestal width of temperature and density *Plasma Phys. Control. Fusion* **54** 105009